JOURNAL OF PROPULSION AND POWER
Vol. 32, No. 3, May-June 2016

Transverse Combustion Instability in a Rectangular Rocket Motor

Pavel P. Popov* and William A. Sirignano†
University of California, Irvine, California 92697

DOI: 10.2514/1.B35868

A computational analysis of transverse acoustic instability is presented for an experimental combustion chamber with rectangular cross section. The analysis is shown to be efficient and accurate. The governing equations are solved on multiple, coupled grids, which are two-dimensional in the combustion chamber and nozzle and one-dimensional in the injector port. Thus, they allow for a fast simulation, even in a serial run. Because of the lengthscale difference, the jet flame behavior at the injectors (including effects of turbulence) can be decoupled from the acoustic effects and solved on a local grid for each jet flame emerging from an injector. Wave propagation through the injector feed ports is evaluated on additional, one-dimensional grids for each injector port. The overall algorithm is used to simulate the Purdue seven-injector rocket engine; good quantitative agreement between simulations and experiment is achieved. All simulations that are predicted to be unconditionally unstable are confirmed by the Purdue experiment. Small perturbations grow to a limit cycle for which the shape is a first transverse acoustic mode of the chamber. Only one result differs from experiment, albeit very slightly.

Nomenclature

a	=	speed of sound, m/s
C_x, C_η	=	rapid-distortion strain of velocity field
c_p	=	specific heat at constant pressure, J/°K · kg
D	=	mass diffusivity, m^2/s
E	=	energy release rate, J/kg · s
L	=	chamber thickness, m
l_m	=	mixing length
p	=	pressure, N/m^2
R_c	=	chamber wall radius of curvature, m
r	=	radial position, m
S_{ij}	=	velocity field strain tensor
T	=	temperature, K
t	=	time, s
Y_F	=	fuel mass fraction
Y_O	=	oxidizer mass fraction
α, β	=	Schwab–Zel'dovich variables
γ	=	Ratio of specific heats
η	=	local radial coordinate for the injector grids
ν_T	=	turbulent kinematic viscosity, m^2/s
ρ	=	density, kg/m^3
ω_i	=	reaction rate of species i, s^{-1}

Subscripts

F	=	fuel
i, j	=	index for Cartesian coordinates
O	=	oxidizer
0	=	undisturbed state

I. Introduction

WE ADDRESS the problem of liquid-propellant rocket engine (LPRE) combustion instability, which is a well-known and undesirable phenomenon in rocket operation. The high energy release by combustion can, in certain conditions, reinforce acoustic oscillations, causing them to grow to destructive amplitudes. LPRE combustion instability provides a very interesting nonlinear dynamics problem, as shown by both theory and experiment: [1–3].

There are two general types of acoustical combustion instability: "driven" instability and "self-excited" instability as noted by Culick [4], who describes evidence in some solid-propellant rockets of the driven type in which noise or vortex shedding causes kinematic waves (i.e., waves carried with the moving gas) of vorticity or entropy to travel to some point where an acoustical reflection occurs. The reflected wave causes more noise or vortex shedding after travelling back, and a cyclic character results. These driven types, which primarily occur in solid rockets, do not rely on acoustical chamber resonance and are much smaller in amplitude than the self-excited instabilities found in liquid-propellant rocket motors [2,5], because the energy level is limited by the driving energy and solid propellants have less chemical energy per unit mass that liquid propellants. The frequency of oscillation for cases in which vortex shedding is a factor depends on two velocities, the sound speed and the subsonic, kinematic speed of the vortex. Consequently, the frequency is lower than a purely acoustic resonant frequency. Oscillations of this type are found in the longitudinal mode; they will not be addressed in this research.

Interest in propellant combinations of hydrocarbon fuel and oxygen, stored as liquids, is returning in the LPRE field. The analysis and results here will address situations in which the hydrocarbon and oxidizer propellants are injected coaxially as gases. These propellants will have elevated temperatures at the injectors because they have been used before injection, either for partial combustion for gas generation to drive a turbo pump or as a coolant before injection. In particular, the inlet temperature and the mean combustion-chamber pressure were carefully chosen to place the mixture in the supercritical (but near perfect gas) domain. Therefore, realism is maintained here when the chamber flow is treated as gaseous and the perfect gas law is used.

The dynamic coupling of the injector system with the combustion chamber of a liquid-propellant rocket engine has been a topic of interest for many decades. Two types of instabilities are known to occur. The chugging instability mode has nearly uniform but time-varying pressure in the combustion chamber. The combustion chamber acts as an accumulator or capacitor while the inflowing propellant mass flux oscillates, because the oscillating chamber pressure causes a flux-controlling oscillatory pressure drop across the injector. This low-frequency instability was characterized by Summerfield [6]. The second type of coupling involves a high frequency oscillation at a near-resonant chamber mode frequency. Here, the resonant frequency has been modestly adjusted because the acoustic system involves some portion of the internal volume of the injector as well as the combustion chamber and convergent nozzle volumes. Crocco and

Presented as Paper 2015-4210 at the 51st AIAA/SAE/ASEE Joint Propulsion Conference, Cleveland, OH, 28–30 July 2015; received 30 April 2015; revision received 14 July 2015; accepted for publication 18 August 2015; published online 7 January 2016.

*Postdoctoral Researcher, Department of Mechanical and Aerospace Engineering.

†Professor, Department of Mechanical and Aerospace Engineering. Fellow AIAA.

Cheng [7] discuss both types of instability for one-dimensional (1-D, or longitudinal) oscillations. Interesting discussions of coupled injector-system acoustics by Nestlerode, Fenwick, and Sack and by Harrje and Reardon can be found in Chapter 3 of the well-known NASA SP-194 [1]. More recent overviews and analyses are provided by Hutt and Rocker [8] and DeBenedictus and Ordonneau [9]. Yang et al. [10] provide several interesting articles on the design and modelling of rocket injector systems.

The disturbances that trigger combustion instability can result from fluid-mechanical disruptions in the propellant injection process, shedding in the combustion chamber of large rogue vortices that eventually flow through the choked nozzle [11], extraordinary excursions in local burning rates [12,13], an acceleration of the entire LPRE engine [12,14], or a synergism amongst such events.

In this paper, an analysis is presented of nonlinear, transverse-mode combustion instability in a rectangular LPRE combustion chamber with a long nozzle, the length of which is comparable to the length of the combustion chamber. Thus, the present study builds on previous analyses [3,12,13]. A particular experimental configuration, the seven-injector rocket engine studied by the Anderson group at Purdue University [15–17], is simulated. The Purdue experimental group studied transverse oscillations in a rectangular cross-section combustion chamber.

Although the rectangular cross-section combustion chamber is not practical for high-pressure operations, it has long been a useful experimental device with easier access for measurements and observations. Reference [1] contains several early works on rectangular cross-section combustion chambers. Bracco and Harrje from Princeton University, and Coultas and Nestlerode from Rocketdyne discuss (in subsections 7.2.4 and 9.2.2.4, respectively) the use of square cross sections for the study of longitudinal modes. Certain observations and measurements were made easier with this cross section. Coultas and Nestlerode discuss their 2-D rocket motor, which takes a rectangular, diametrical slice of an actual motor (subsection 9.2.2.5). Sirignano presents a generalized, 3-D, linear theory and applies it to several combustion chamber shapes for transverse oscillations (subsection 3.5.1); rectangular cross sections are considered there. Levine [18] expounds on the Rocketdyne experience with the 2-D motor. With various practical propellant combinations, stable and unstable operational domains were found; transverse oscillations could be triggered.

In practice, propellant flow through the injector can be in the same liquid phase as the stored propellant, in a gaseous form mixed with combustion products because of upstream flow through a preburner used for a propellant turbopump, or in gaseous form because the liquid propellant was used as a combustion-chamber-wall coolant upstream. We consider here gaseous coaxial flow of the pure propellants, RP1, ethane, and hydrogen peroxide, based on the last scenario. In the experimental study, RP1 is still in the liquid phase at the injector's exit, and its vaporization is not modeled here.

The remainder of this paper is organized as follows: the experimental setup for the seven-injector rocket engine is presented in Sec. II, the governing equations of the pressure wave dynamics are given in Sec. III. Section IV presents the calculation of heat release performed on local cylindrical grids for each injector. Computational results are given in Sec. V, and a brief discussion on the computational cost of this procedure is provided in Sec. VI. Finally, conclusions are drawn in Sec. VII.

II. Experimental Configuration and Results

The Purdue combustion chamber is shown in Fig. 1. Its upstream portion is rectangular, of length 13.39 cm, width 26.67 cm, and height 3.81 cm. This is followed by a straight converging nozzle of length 9/84 cm, the throat of which has a cross section of 15.07 cm× 1.44 cm.

The injector plate contains seven injectors spaced apart evenly in the transverse direction, with a distance of 3.81 cm between adjacent injector axes. Each injector consists of an oxidizer post coaxial with a surrounding fuel inlet, with the oxidizer post diameter being 2.05 cm and the fuel inlet outer diameter being 2.31 cm, with an inner diameter of 2.229 cm. For the central study injector, the length of the oxidizer post is 12.92 cm, and the length of the fuel inlet is 2.79 cm; for the driving injectors, the length of the oxidizer post is 17.04 cm, and the length of the fuel inlet is 2.28 cm.

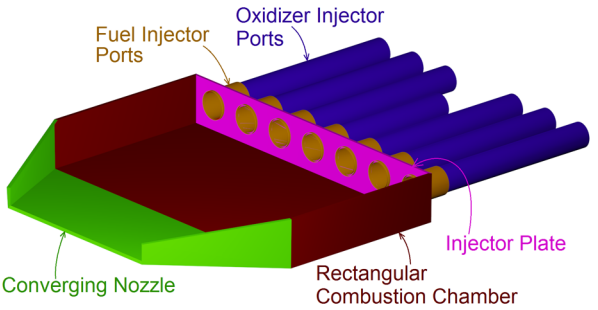

Fig. 1 Rectangular combustion chamber and nozzle with injectors.

The oxidizer mixture for the central study element is 90% hydrogen peroxide, which is partially decomposed at the beginning of the oxidizer post and fully decomposed by the time it reaches the combustion chamber orifice. Thus, the inlet mixture in the combustion flame grids is, on a mass basis, 58% H_2O and 42% O_2, for an H_2O mass flow rate of 0.106 kg/s and an O_2 mass flow rate of 0.076 kg/s; the inlet temperature is 1029 K. The fuel mixture for the study element is ethane, with a mass flow rate of 0.025 kg/s and an inlet temperature of 319 K.

The oxidizer mixture for the driving elements element is again 58% H_2O and 42% O_2, with an H_2O mass flow rate of 0.113 kg/s, an O_2 mass flow rate of 0.083 kg/s, and an inlet temperature of 1029 K. The fuel mixture for the driving elements is RP1, with a mass flow rate of 0.033 kg/s and an inlet temperature of 298.15 K. Decane will be used in our model to represent the RP1. In this study, we simulate several of the experimental configurations studied by the Anderson group, in particular the configurations OOXOXOO, OXXOXXO, XOOOOOX, and XOXOXOX, in which an "X" indicates an injector port with only oxidizer inflow (i.e., the fuel ports for that injector are plugged) and "O" indicates an injector port with both fuel and oxidizer. In all of these configurations, the central study element has ethane fuel inflow, and the difference amounts to which of the driving elements have RP1 fuel inflow.

With this experimental configuration, a spontaneous instability of peak-to-peak amplitude of 620 kPa is measured, with a mean pressure of 965 kPa. Time histories of pressure can be found on Fig. 8 is on page 9 of [17]. The frequency of the first transverse mode component of the instability is 2032 Hz.

III. Basic Equations for Wave Dynamics

The equations for pressure and velocity in the chamber are simplified: the scale of turbulent motions is considered to be much smaller than the acoustic wave scale, the lengthscale of which is comparable to the lengthscale of the combustion chamber. Thus, it can be assumed that turbulence and molecular diffusion do not have a significant impact on the large-scale pressure and velocity wave fields, which can then be solved in inviscid form.

A. Three-Dimensional Wave Equations

Following the developments in [3], the large-scale pressure wave equation has the form.

$$\frac{\partial^2 p}{\partial t^2} - a^2 \frac{\partial^2 p}{\partial x_j \partial x_j} = \frac{\partial \rho}{\partial t}\frac{\partial a^2}{\partial t} + (\gamma - 1)\frac{\partial E}{\partial t} + a^2 \frac{\partial^2 (\rho u_j u_i)}{\partial x_i \partial x_j} \quad (1)$$

The left side of the equation represents the wave operator in three dimensions. The second term on the right represents the influence of the combustion energy release on the acoustic instability and is thus an integral component of the study of rocket engine instability.

The large-scale velocity components evolve by

$$\frac{\partial u_i}{\partial t} + u_j \frac{\partial u_i}{\partial x_j} + \frac{C}{p^{1/\gamma}} \frac{\partial p}{\partial x_i} = 0 \tag{2}$$

in which $C = p_0^{1/\gamma}/\rho_0$, and the assumption is made that pressure dominates over the turbulent and molecular viscosity terms.

These equations, applied previously to a cylindrical chamber [3,12,13], were successful in identifying three domains within the parameter space: unconditional instability, conditional instability, and unconditional stability. Transients and limit cycles were produced for several different instability events.

B. Reduction to a Two-Dimensional Wave Equation

In this study, we use the fact that the combustion chamber is narrow in the height dimension, which implies that the solution fields vary little in that dimension and can therefore be averaged over it. The chamber height $L(x, y)$ is constant over the initial section of the combustion chamber and varies linearly with x in the converging nozzle portion of the chamber.

Following Sirignano and Popov [3], 2-D averages (here, over the height dimension) of the pressure and velocity fields

$$\tilde{p} = (1/L(x,y)) \int_0^{L(x,y)} p \, \mathrm{d}x_3, \quad \tilde{\rho} = (1/L(x,y) \int_0^{L(x,y)} \rho \, \mathrm{d}x_3,$$

$$\tilde{a} = (1/L(x,y)) \int_0^{L(x,y)} a \, \mathrm{d}x_3, \quad \text{and} \quad \tilde{\boldsymbol{u}} = (1/L(x,y)) \int_0^{L(x,y)} \boldsymbol{u} \, \mathrm{d}x_3$$

Integrating Eq. (1) over x_3 and neglecting the difference between products of averages and averages of products, we get

$$\frac{\partial^2 \tilde{p}}{\partial t^2} - \tilde{a}^2 \left[\frac{\partial^2 \tilde{p}}{\partial x_j \partial x_j} + \frac{1}{L} \frac{\partial L}{\partial x_1} \frac{\partial \tilde{p}}{\partial x_1} \right] = \frac{\partial \tilde{p}}{\partial t} \frac{\partial \tilde{a}^2}{\partial t} + (\gamma - 1) \frac{\partial \tilde{E}}{\partial t} + \\ + \tilde{a}^2 \frac{\partial^2 (\tilde{\rho} \tilde{u}_j \tilde{u}_i)}{\partial x_i \partial x_j} + \tilde{a}^2 \frac{1}{L} \frac{\partial L}{\partial x_1} \frac{\partial (\tilde{\rho} \tilde{u}_1 \tilde{u}_i)}{\partial x_i} \tag{3}$$

in which $i = 1, 2$ and $j = 1, 2$. The last terms on both the left and right sides correspond to the effect which the variable combustion chamber width (in the x_3 direction) has on the divergence operators in Eq. (1). The preceding equation contains derivatives of L only in the x_1 direction, because L does not vary in the x_2 direction.

Similarly, the averaged version of Eq. (2) has the form

$$\frac{\partial \tilde{u}_i}{\partial t} + \tilde{u}_j \frac{\partial \tilde{u}_i}{\partial x_j} + \frac{1}{L} \frac{\partial L}{\partial x_1} (\tilde{u}_i \tilde{u}_1) + \frac{C}{\tilde{p}^{1/\gamma}} \frac{\partial \tilde{p}}{\partial x_i} = 0 \tag{4}$$

These equations are solved on an orthogonal curvilinear coordinate system, which represents a conformal map of the present hexagonal domain onto a square. The curvilinear form of Eqs. (3) and (4), with the associated nomenclature, is given in Appendix A.

At the walls of the combustion chamber, the boundary conditions on the pressure and velocity are

$$\tilde{u}_n = 0; \qquad \frac{\partial \tilde{p}}{\partial n} = \frac{\tilde{p}^{1/\gamma} \tilde{u}_t^2}{C R_c} \tag{5}$$

with $\tilde{u}_n$ and $\tilde{u}_t$, respectively, denoting the components of velocity normal and tangential to the wall boundary, and R_c denoting the wall boundary's radius of curvature. At the downstream end of the convergent nozzle, a Mach number $M = 0.9$ is enforced, and the short nozzle approximation is used to represent the additional convergence to a choked throat, as an approximation to the sonic condition in the experiment. This is done in order to ensure the numerical stability of the compressible solver algorithm. Because the longitudinal distance between the points of $M = 0.9$ and 1.0 is small compared with the acoustic wavelength, the approximation is suitable for the present analysis.

IV. Determination of Heat Release Rate E with Coaxial Injection

We seek to model the heat release rate of change $\partial E/\partial t$, which is an integral component to the acoustic instability pressure wave equation, Eq. (1). Following [3], we shall denote $\alpha = Y_F - \nu Y_O$, in which Y_F and Y_O are the fuel and oxidizer mass fractions and ν is their stoichiometric ratio. Then, α is a conserved scalar, which we will determine in the vicinity of each injector on an axisymmetric cylindrical grid with the assumption that the injector flow field is mostly in the direction coaxial to the injector. An illustration of the grids used for the jet flames emerging from the seven injectors, and their relation to the combustion chamber grid, is given in Fig. 2.

With the variable β being defined by $\beta = (Q/(c_p T_o))Y_F + T/T_o - (p/p_o)^{(\gamma-1)/\gamma}$, where Q is the fuel's specific chemical energy, the evolution equations for the variables α, β, and Y_F have the following form:

$$\frac{\partial \alpha}{\partial t} + u_x \frac{\partial \alpha}{\partial x} + u_\eta \frac{\partial \alpha}{\partial \eta} - D \left[\frac{\partial^2 \alpha}{\partial \eta^2} + \frac{1}{\eta} \frac{\partial \alpha}{\partial \eta} + \frac{\partial^2 \alpha}{\partial x^2} \right] = 0 \tag{6}$$

$$\frac{\partial \beta}{\partial t} + u_x \frac{\partial \beta}{\partial x} + u_\eta \frac{\partial \beta}{\partial \eta} - D \left[\frac{\partial^2 \beta}{\partial \eta^2} + \frac{1}{\eta} \frac{\partial \beta}{\partial \eta} + \frac{\partial^2 \beta}{\partial x^2} \right] = 0 \tag{7}$$

and

$$\frac{\partial Y_F}{\partial t} + u_x \frac{\partial Y_F}{\partial x} + u_\eta \frac{\partial Y_F}{\partial \eta} - D \left[\frac{\partial^2 Y_F}{\partial \eta^2} + \frac{1}{\eta} \frac{\partial Y_F}{\partial \eta} + \frac{\partial^2 Y_F}{\partial x^2} \right] = \omega_F \tag{8}$$

in which x and η, respectively, are the axial and radial coordinates of the cylindrical injector grids, and the source term on the right side of Eq. (8) is obtained from a Westbrook–Dryer two-step oxidation mechanism [19], from the fuel (C_2H_6 for the central injector element, $C_{10}H_{22}$ for the driving injector elements) to CO, and then from CO to CO_2. To obtain the concentrations of both the injector fuel and CO from the fuel mass fraction, it is assumed that oxidation of CO occurs only after the partial oxidation of the fuel to CO has reached its completion. This simple two-step mechanism does not allow for the presence of common combustion radicals, such as OH, and therefore would lead to an overprediction of the flame temperature. Because of the considerable amount of water vapor in the oxidizer flow, however, this overprediction of temperature is expected to be on the order of 5% and will not have a significant impact on the sound speed within the combustion chamber.

Building on Sirignano and Popov [3], the source term in Eq. (8) is obtained via an assumed probability density function (PDF) method model for α and β, so that the means of α and β evolve by Eqs. (6) and (7) and their subgrid distributions are assumed to be beta functions, which are standard PDFs for modeling mixing of two or more streams. The term ω_F in Eq. (8) is then obtained via integration over the sample space of α and β. The assumed PDF model has been used with great success for the simulation of turbulent nonpremixed

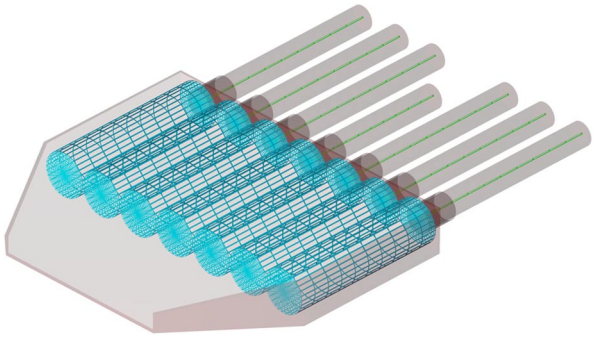

Fig. 2 Cylindrical jet flame grids (wireframe mesh) and 1-D injector port grids situated within the rocket engine.

flames, which are not near extinction [20]. For more details, the reader is referred to [20].

The axial and radial velocities in Eqs. (6–8) are obtained from a solution of the variable density Reynolds-averaged Navier–Stokes axisymmetric equations:

$$\rho\left(\frac{\partial u_x}{\partial t}+u_x\frac{\partial u_x}{\partial x}+u_\eta\frac{\partial u_x}{\partial \eta}\right)=-\frac{\partial p_l}{\partial x}+\rho\nu_T\left[\frac{\partial^2 u_x}{\partial x^2}+\frac{1}{\eta}\frac{\partial}{\partial \eta}\left(\eta\frac{\partial u_x}{\partial \eta}\right)\right] \tag{9}$$

$$\rho\left(\frac{\partial u_\eta}{\partial t}+u_x\frac{\partial u_\eta}{\partial x}+u_\eta\frac{\partial u_\eta}{\partial \eta}\right)=-\frac{\partial p_l}{\partial \eta}+\rho\nu_T\left[\frac{\partial^2 u_\eta}{\partial x^2}+\frac{1}{\eta}\frac{\partial}{\partial \eta}\left(\eta\frac{\partial u_\eta}{\partial \eta}\right)-\frac{u_\eta}{\eta^2}\right] \tag{10}$$

which are solved on each jet flame grid, in which $p_l(x,\eta,t)$ is a local hydrodynamic pressure for which the mean is, by definition, 0 and which has considerably lower magnitude than the injector pressure $p(t)$ obtained from Eq. (1). The density in Eqs. (10) and (11) is obtained from the species scalars and the long-wavelength pressure $p(t)$ at the injector's location, so that the overall procedure for solving Eqs. (10) and (11) is elliptic.

The turbulent viscosity ν_T is evaluated based on a mixing-length model [21]:

$$\nu_T = l_m^2(2\tilde{S}_{ij}\tilde{S}_{ij})^{(1/2)} \tag{11}$$

in which $\tilde{S}_i j$ is the strain tensor of the velocities in Eqs. (10) and (11) and l_m is the mixing length, defined as

$$l_m(x)=\frac{3}{1+C_x(x)+C_\eta(x)}r_{1/2}(x) \tag{12}$$

In the preceding formula, $r_{1/2}(x)$ is the radius in the constant x plane at which the velocity magnitude has decreased to $1/2$ of its maximum value, and $C_x(x)$, $C_\eta(x)$ are the values of strain of the approximately axisymmetric velocity fields of Eqs. (10) and (11) by the chamber velocity obtained in solution to Eq. (4). Utilizing rapid-distortion theory (RDT) [21], the fluctuating velocity field evolves and is driven by the mean strain when the time scale of the mean strain is much faster than that of the turbulence. Hence, C_x, C_η evolve by

$$\frac{\mathrm{d}C_x(x)}{\mathrm{d}t}=C_x(x)\frac{\partial\tilde{u}_1}{\partial x_1}+(1-C_x(x))(2\tilde{S}_{ij}\tilde{S}_{ij})^{(1/2)} \tag{13}$$

$$\frac{\mathrm{d}C_\eta(x)}{\mathrm{d}t}=C_\eta(x)\frac{\partial\tilde{u}_2}{\partial x_2}+(1-C_\eta(x))(2\tilde{S}_{ij}\tilde{S}_{ij})^{(1/2)} \tag{14}$$

in which the velocity strain terms $\partial\tilde{u}_1/\partial x_1$ and $\partial\tilde{u}_2/\partial x_2$ are evaluated at the point in the combustion chamber grid that corresponds to the point at a distance of x along the injector grid's centerline. As we shall see in Sec. V, the use of the rapid-distortion correction improves the agreement of the computational results with experiments: without it, the underprediction of the oscillation amplitude is much more pronounced.

Finally, following Popov, Sideris, and Sirignano [12], the pressure and velocity in the injector posts are solved via the set of 1-D wave equations:

$$\frac{\partial^2 p}{\partial t^2}-a^2\frac{\partial^2 p}{\partial x^2}=a^2\frac{\partial^2(\rho u^2)}{\partial x^2}-\frac{\partial a^2}{\partial t}\frac{\partial(\rho u)}{\partial x} \tag{15}$$

$$\frac{\partial u}{\partial t}+u\frac{\partial u}{\partial x}=-\frac{1}{\rho}\frac{\partial p}{\partial x} \tag{16}$$

They are solved on a 1-D grid upstream of each cylindrical injector grid (shown in Fig. 2). In this model, velocity fluctuations affect the energy release rate through the modification of the eddy diffusivity, mixing rate, and rate of propellant inflow into the combustion chamber. Pressure fluctuations, on the other hand, affect the chemical rate and drive the injector port velocity fluctuations.

V. Results

With the simulation procedure described here, it was found that the seven-injector combustion chamber is unconditionally unstable for all experimental cases with the exception of the XOXOXOX case, which is conditionally unstable. For the rest of the cases, arbitrarily small perturbations grow to a limit cycle for which the major component is the first transverse mode of the chamber in the x_2 direction.

Figure 3 shows a contour plot of the pressure field in a fully-developed limit cycle oscillation for the most unstable OOXOXOO case. Two different perturbation mechanisms were tested: the first consisted of setting an initial condition that is a first transverse mode pressure wave of low amplitude, whereas the second consisted of the imposition on the combustion chamber of a reciprocating acceleration in the transverse, x_2 direction. As can be seen in Fig. 3, both disturbance mechanisms produced the same instability waveform, which indicates that, for this setup, the shape of the limit cycle does not depend on the initial condition.

It was found that the limit cycle does not produce shocks; upon grid refinement the pressure gradients in the transverse direction do not increase. This is consistent with the experimental findings of Shipley et al. [17], which did not discover the existence of shocks in the experimentally measured instability. For the OOXOXOO case, a contour plot of the temperature field for the ethane injector is given in Fig. 4. As can be seen on that plot, the maximum flame temperature is 2890 K, with a coflow temperature of 2660 K, which is in good agreement with the numerical results of Shipley et al. [17], who report

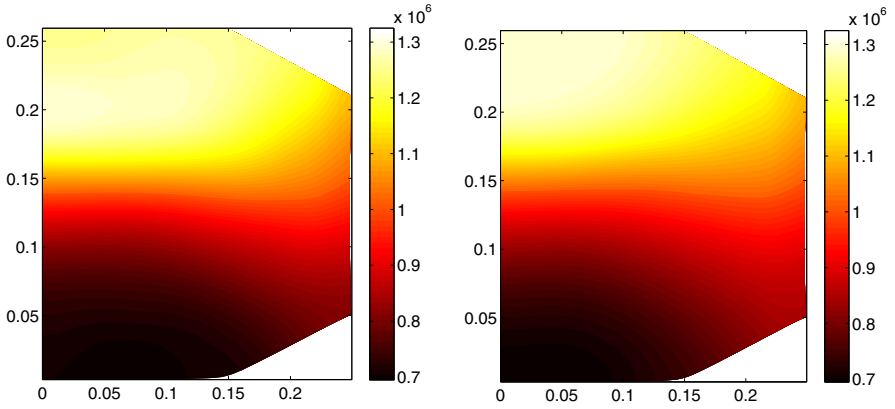

Fig. 3 Pressure contours for acoustic limit cycles for the seven-injector rocket engine. (Left) A limit cycle caused by an incited low-amplitude pressure wave. (Right) A limit cycle caused by reciprocating acceleration.

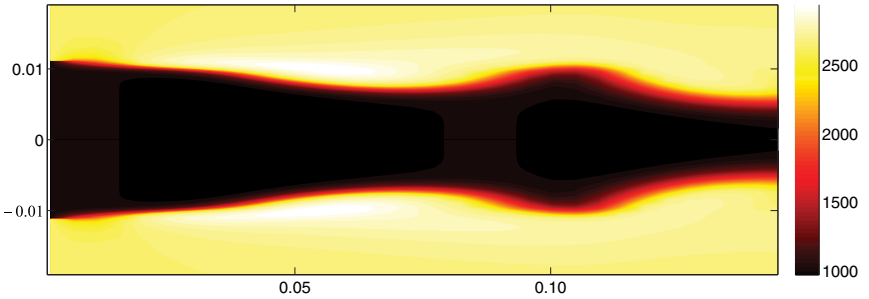

Fig. 4 Temperature contour plots for the center injector (OOXOXOO case). The fuel for this injector is C_2H_6.

a maximum temperature of approximately 2800 K and a coflow temperature of approximately 2550 K.

To illustrate the time-dependent nature of the solution, Fig. 5 plots (for the OOXOXOO case) the calculated pressure over four cycle periods at four different locations: at the outlet of the central (study) injector, at the outlet of one of the outermost driving injectors, at the center of the nozzle, and at the edge of the nozzle. The power spectrum density of the pressure signals is also shown, with peaks at the 1931 Hz frequency and its harmonics. It can be seen that the leading edge of the pressure wave has a sharper gradient than its trailing edge, but the gradient is still finite. Note that, although the central injector falls at a pressure node of the linear first transverse acoustic mode, there is still some pressure oscillation at that location, due to higher-order effects. We also note that the pressure oscillations at the central injector are out of phase with the larger amplitude oscillations near the side wall.

Finally, comparing the pressure time histories of Fig. 5 to their experimental counterparts shown in Fig. 8 is on page 9 of [17], we see that the present numerically calculated time histories of pressure are smoother than the experimental measurements; it is also observed

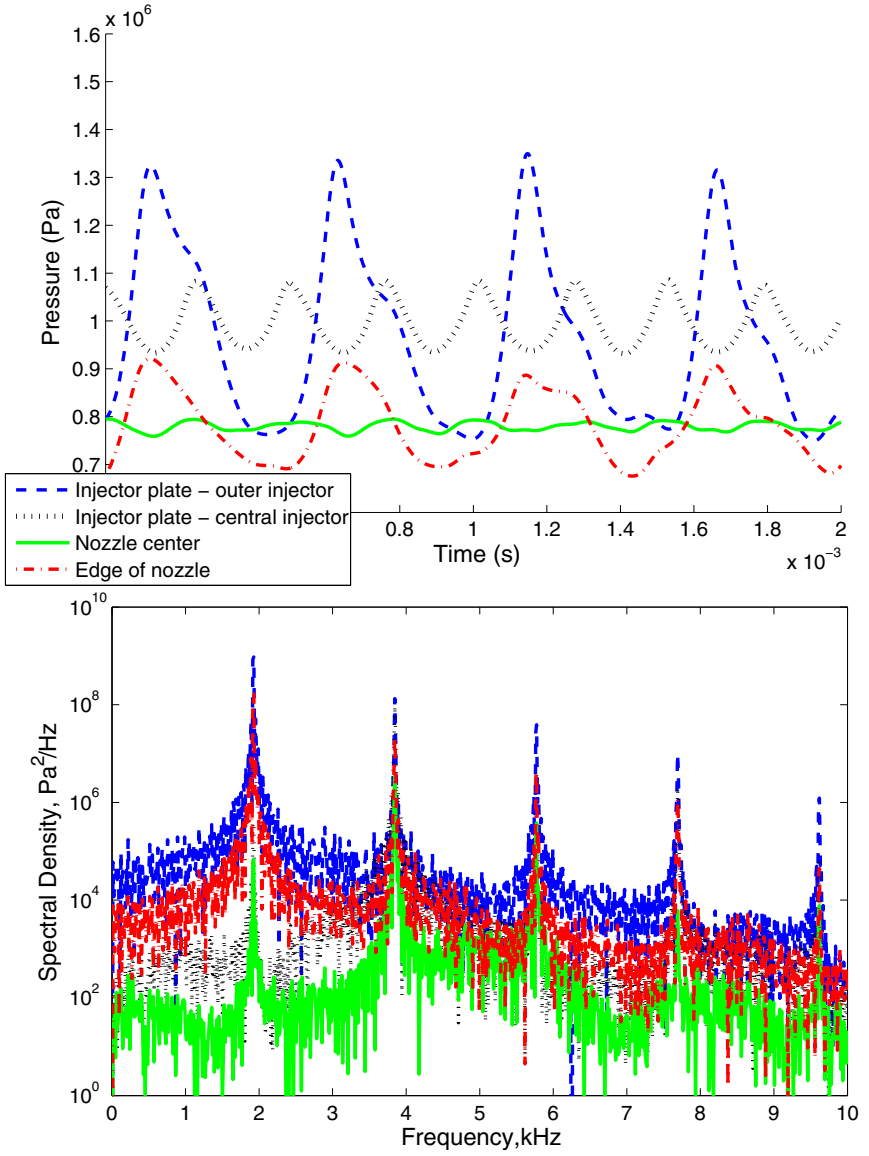

Fig. 5 Top: pressure as a function of time at four different points in the domain ("OOXOXOO" case). Bottom: power spectrum density plots of the pressure time histories, showing peaks at the 1931 Hz frequency and its harmonics.

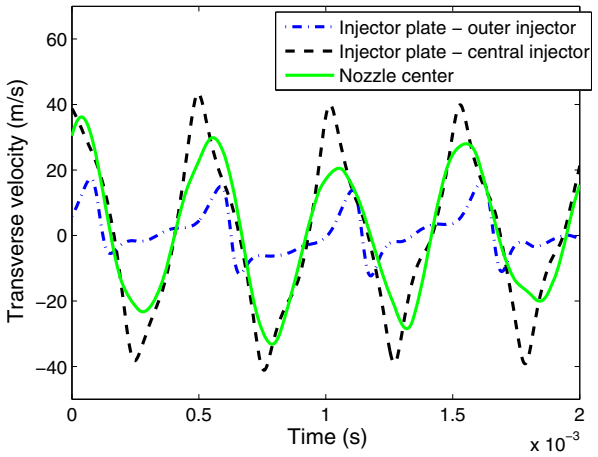

Fig. 6 Transverse velocity as a function of time at three different points in the domain (OOXOXOO case).

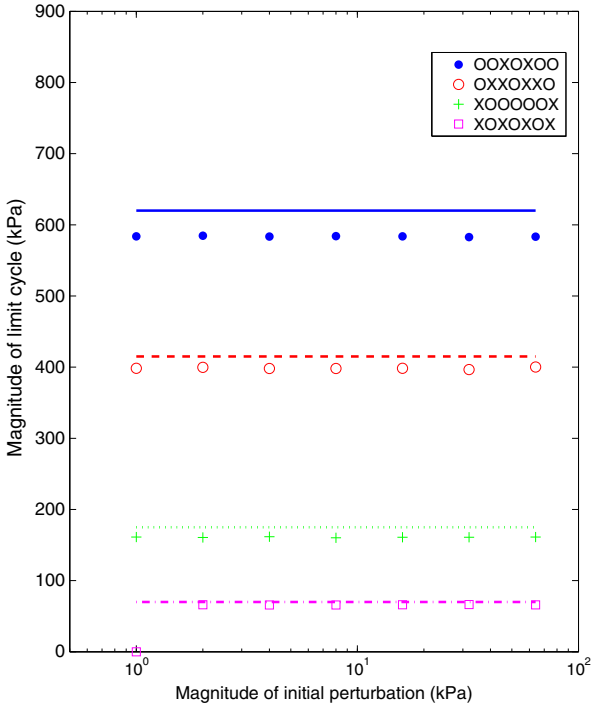

Fig. 8 Limit-cycle amplitudes for simulations in which initial condition is a first transverse mode pressure wave of varying amplitude. The lines indicate the experimentally observed limit-cycle amplitudes.

that the power spectral density away from the first transverse frequency and its harmonics has a lower magnitude. This can be attributed to the fact that the present study is of a 2-D nature, and the smaller 3-D turbulent structures are not represented.

For the OOXOXOO" case, Fig. 6 plots the transverse velocity at the central and outer injector and at the center of the nozzle. We note that the transverse velocity is greatest at the central injector, which falls on a velocity antinode of the linear first transverse mode. Time histories of the net heat releases from the central and outer driving injector are given in Fig. 7. For the driving injector, we can see considerable large amplitude oscillation of the heat release over time. It is this variation that drives the transverse acoustic instability. The stronger response of the heat release rate near the outer injector versus the inner injector implies that pressure coupling, either directly or via wave propagation in the injectors, is stronger than velocity coupling of the energy release rate. The coupling of pressure or velocity with the energy release is two way. The pressure and velocity histories at the flame affect the local energy release rate. The energy release rate at the flame has a global effect on pressure and velocity throughout the chamber, manifesting as a source term in the pressure wave equation.

Additional comparisons with experimental data can be made with respect to the frequency and amplitude of the limit cycle. Figure 8 plots the eventual limit cycle magnitudes, for the different experimental cases, of simulations in which the initial condition is a first transverse mode wave of varying initial amplitude.

As can be seen on that figure for the cases OOXOXOO, OXXOXXO, and XOOOOOX, all initial perturbations down to a magnitude of 1 kPa produce a limit cycle for which the amplitude is constant for the given test case. For the XOXOXOX case, an initial

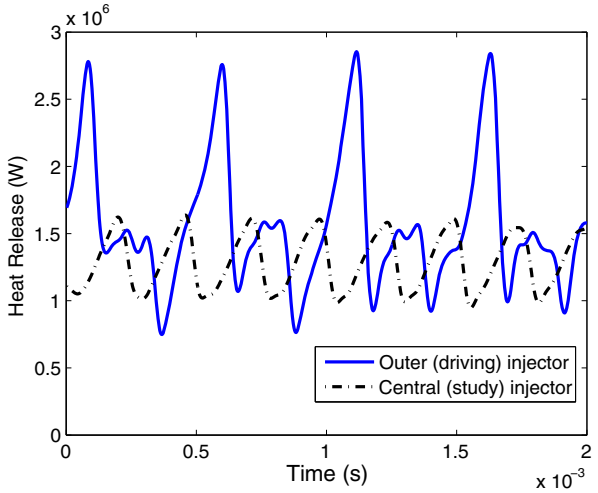

Fig. 7 Net heat release, as a function of time, of the central and outermost driving injectors (OOXOXOO case).

perturbation of amplitude 1 kPa will decay, whereas perturbations of amplitude 2 kPa will grow to an acoustic limit cycle. Thus, our simulation procedure predicts that the first three cases mentioned above are unconditionally unstable, which is in agreement with the experimental data (in the experiment, the instability developed spontaneously, without the need for forcing), and the XOXOXOX case is conditionally unstable, contrary to experimental data. Both the simulations and the experiment indicate that the XOXOXOX case is close to the physical bifurcation in the operational domain known commonly as the linear stability limit. Thus, some difference between experiment and computation here is to be expected; the overall trend is properly predicted.

Despite this disagreement for the XOXOXOX case, overall the present simulation predicts the stability characteristics of the seven-injector rocket motor exceptionally well. The limit-cycle amplitudes and frequencies for the four cases (in those simulations in which a limit cycle was observed) are given in Table 1.

As can be seen in this table, the present computational procedure tends to underpredict both the amplitude and frequency of the experimentally observed limit cycles. In terms of frequency, the numerical results are consistently between 5 and 6% lower than experimental results. The relative error in the limit-cycle amplitude varies more, with the maximum being 8% and the minimum being 4%. We also note that the disagreement in amplitude and frequency tends to be greater in the more stable cases, XOOOOOX and XOXOXOX. Overall, however, the quantitative agreement is strong (6.25% mean relative error for amplitude, 5.25% mean relative error for frequency) for a simulation procedure such as the present, optimized for low computational cost, for design purposes.

We also note that the use of the RDT model encapsulated by Eqs. (12–14) contributes to the good agreement between experiment and simulation: without RDT, the simulated limit-cycle amplitudes are 543, 379, 157, and 66 kPa for the OOXOXOO, OXXOXXO, XOOOOOX, and XOXOXOX cases, respectively. Thus, especially in the cases with a large limit-cycle amplitude, the underprediction of experimental results would be considerably more pronounced without the incorporation of the RDT model. Because the RDT model allows us to model the nonaxisymmetric straining of the injector flames by the transverse pressure waves and the effect of this strain on the injector

Table 1 Comparison between computed and experimentally observed limit cycle amplitudes and frequencies

Test case	Simulation limit-cycle amplitude, kPa	Experimental limit-cycle amplitude, kPa	Simulation frequency, Hz	Experimental frequency, Hz	Relative errors (amplitude / frequency; %/%)
OOXOXOO	580	620	1931	2032	6/5
OXXOXXO	398	415	1720	1807	4/5
XOOOOOX	161	175	1766	1855	8/5
XOXOXOX	65	70	1803	1912	7/6

Table 2 Effects of oxidizer mass flow variation on the stability characteristics of the OOXOXOO case

Test case stability regime	H_2O mass flow rate, kg/s	O_2 mass flow rate, kg/s	Limit-cycle amplitude, kPa
Unconditionally unstable	0.113	0.083	580
Conditionally unstable	0.079	0.058	213
Unconditionally stable	0.0565	0.0415	0

flames' turbulent combustion, the superior performance of the simulation with the RDT model is consistent with expectations.

Finally, we note that the stability regime of the combustion chamber can be greatly affected by modifying the injector mass flow away from the reported experimental values. As shown in Table 2, reducing the oxidizer mass flow of the outer driving injectors of the OOXOXOO case to 70% of the experimental values yields a conditionally unstable simulation: a limit cycle oscillation of 213 kPa amplitude is predicted but only for first transverse mode perturbations with amplitude 98 kPa or greater. Further reducing the oxidizer mass flow rate to 50% of the experimental values leads to an unconditionally stable regime.

VI. Computational Cost

The main advantage of the present computational procedure over existing numerical algorithms is in its very low computational cost. Because of the fact that the governing equations were simplified to a form that could be solved on coupled sets of 2-D and 1-D grids, each of the simulations run for this study took approximately 1000 s in serial implementation. Combined with the reasonable prediction of the combustion chamber's stability characteristics, this makes the present computational procedure a useful tool in exploring the stability characteristics of a given rocket engine and in developing design strategies for stability, from both a passive and an active control viewpoint.

VII. Conclusions

The computational procedure previously developed in Sirignano and Popov [3] and Popov, Sideris, and Sirignano [12] for the simulation of transverse combustion instabilities in a cylindrical rocket motor has been extended for use in rectangular, long-nozzle rocket motors. The theoretical extensions include the use of RDT, coupling of diffusivity with transverse velocity, an assumed-PDF flamelet model that estimates subgrid mixing, and unsteady nozzle flow. The algorithm was applied to the Purdue seven-injector rocket engine experiment, and it was discovered that three of the configurations were unconditionally unstable, with the smallest perturbations growing to an instability. One other configuration was conditionally unstable, requiring a modest trigger.

The shape of the limit cycle, which is a first transverse mode, is independent of the destabilizing event. Reasonable quantitative agreement between the computational model and experimental results was achieved, with a mean relative error (across the four test cases) of 5.25% in the frequency of the limit cycle and a mean relative error of 6.25% in the limit cycle amplitude. Finally, based on a comparison of the heat release fluctuations between the central and outer injectors, it is determined that pressure oscillations have a stronger effect on the energy release rate than do oscillations of the transverse velocity.

Appendix: Differential Equations for Pressure and Velocity in Curvilinear Coordinates

Here, we present the form of Eqs. (3) and (4), which is solved on the combustion chamber pressure and velocity orthogonal curvilinear grid. We use the variables q^1 and q^2 to denote the coordinates of the curvilinear grid. Then, using h_i to denote the Lamé coefficients, with $J = h_1 h_2$, using g_{ij} and g^{ij}, respectively, to denote the covariant and contravariant metric tensors and Γ^k_{ij} to denote the Christoffel symbols of the second kind, the curvilinear form of Eq. (3) is

$$\frac{\partial^2 \tilde{p}}{\partial t^2} - \tilde{a}^2\left[\frac{1}{J}\frac{\partial}{\partial q^i}\left(\frac{J}{h^2_{(i)}}\frac{\partial \tilde{p}}{\partial q^i}\right) + \frac{1}{L}\frac{\partial L}{\partial q^i}\frac{g^{ji}}{h_{(i)}}\frac{1}{h_{(j)}}\frac{\partial \tilde{p}}{\partial q^j}\right] = \\ = \frac{\partial \tilde{\rho}}{\partial t}\frac{\partial \tilde{a}^2}{\partial t} + (\gamma - 1)\frac{\partial \tilde{E}}{\partial t} \\ + \tilde{a}^2\frac{1}{J}\frac{\partial}{\partial q^i}\left\{\left[\frac{\partial \tilde{\rho}\tilde{u}_m\tilde{u}_j}{\partial q^k} - \Gamma^l_{km}\tilde{\rho}\tilde{u}_l\tilde{u}_j - \Gamma^l_{kj}\tilde{\rho}\tilde{u}_m\tilde{u}_l\right]g^{mk}g^{ij}\frac{J}{h_{(i)}}\right\} + \\ + \tilde{a}^2\frac{1}{L}\frac{\partial L}{\partial q^i}\frac{g^{ji}}{h_{(i)}}\left[\frac{\partial \tilde{\rho}\tilde{u}_m\tilde{u}_j}{\partial q^k} - \Gamma^l_{km}\tilde{\rho}\tilde{u}_l\tilde{u}_j - \Gamma^l_{kj}\tilde{\rho}\tilde{u}_m\tilde{u}_l\right]g^{mk} \qquad \text{(A1)}$$

in which in the preceding equation indices with braces, such as (i), are not summed over. Similarly, the curvilinear form of Eq. (4) is

$$\frac{\partial \tilde{u}_i}{\partial t} + \left[\frac{\tilde{u}_k}{h_{(k)}}\frac{\partial \tilde{u}_i}{\partial q^k} + \frac{\tilde{u}_k}{h_{(k)}h_{(i)}}\left(\tilde{u}_i\frac{\partial h_{(i)}}{\partial q^k} - \tilde{u}_k\frac{\partial h_{(k)}}{\partial q^i}\right)\right] + \\ + \frac{1}{h_{(k)}L}\frac{\partial L}{\partial q^k}g^{kj}(\tilde{u}_i\tilde{u}_j) + \frac{C}{\tilde{p}^{1/\gamma}h_{(i)}}\frac{\partial \tilde{p}}{\partial q^i} = 0 \qquad \text{(A2)}$$

The 2-D coordinates are equivalently the solutions of the Laplace equation. Thereby, they follow the streamlines and potential flow lines of a fictitious incompressible potential flow in the same chamber and convergent nozzle.

Acknowledgments

This research was supported by the Air Force Office of Scientific Research under Grant FA9550-12-1-0156, with Mitat Birkan as the Program Manager.

References

[1] Harrje, D., and Reardon, F., "Liquid Propellant Rocket Combustion Instability," NASA SP-194, U.S. Government Printing Office, 1972.

[2] Oefelein, J. C., and Yang, V., "Comprehensive Review of Liquid-Propellant Combustion Instabilities in F-1 Engines," *Journal of Propulsion and Power*, Vol. 32, No. 1, 1993, pp. 657–677. doi:10.2514/3.23674

[3] Sirignano, W. A., and Popov, P. P., "Two-Dimensional Model for Liquid-Rocket Transverse Combustion Instability," *AIAA Journal*, Vol. 51, No. 12, 2013, pp. 2919–2934. doi:10.2514/1.J052512

[4] Culick, F. E. C., *Unsteady Motions in Combustion Chambers for Propulsion Systems*, AGARDograph AG-AVT-039, North Atlantic Treaty Organization, Neuilly-Sur-Seine, France, 2006.

[5] Prevost, M., Vuillot, F., and Traineau, J. C., "Vortex Shedding Driven Oscillations in Subscale Motors for the Ariane 5 MPS P230," *32nd AIAA/ASME/SAB/ASEE Joint Propulsion Conference and Exhibit*, AIAA Paper 1996-3247, 1996.

[6] Summerfield, M., "A Theory of Unstable Combustion in Liquid Propellant Rocket Motors," *Journal of the American Rocket Society*,

Vol. 21, No. 1, 1951, pp. 108–114.
doi:10.2514/8.4395

[7] Crocco, L., and Cheng, S.-I., *Theory of Combustion Instability in Liquid Propellant Rocket Motors*, AGARD Monograph 8, Buttersworth, London, 1956.

[8] Hutt, J. J., and Rocker, M., "High-Frequency Injector-Coupled Combustion Instability," *Liquid Rocket Engine Combustion Instability*, edited by Yang, V., and Anderson, W., Vol. 169, Progress in Astronautics and Aeronautics, AIAA, New York, 1995, pp. 345–376.

[9] DeBenedictus, M., and Ordonneau, G., "High Frequency Injection Coupled Combustion Instabilities Study of Combustion Chamber/Feed System Coupling," *Joint Propulsion Conference*, AIAA Paper 2006-4721, 2006.

[10] Yang, V., Habiballah, M., Hulba, J., and Popp, M., *Liquid Rocket Combustion Devices: Aspects of Modeling, Analysis, and Design*, Vol. 200, Progress in Astronautics and Aeronautics, AIAA, Reston, VA, 2005, pp. 1–165.

[11] Swithenbank, J., and Sotter, G., "Vortex Generation in Solid Propellant Rocket," *AIAA Journal*, Vol. 2, No. 7, 1964, pp. 1297–1302.
doi:10.2514/3.2535

[12] Popov, P. P., Sideris, A., and Sirignano, W. A., "Propellant Injector Influence on Liquid Propellant Rocket Engine Instability," *Journal of Propulsion and Power*, Vol. 31, No. 1, 2015, pp. 320–331.
doi:10.2514/1.B35400

[13] Popov, P. P., Sideris, A., and Sirignano, W. A., "Stochastic Modelling of Transverse Wave Instability in a Liquid Propellant Rocket Engine," *Journal of Fluid Mechanics*, Vol. 745, 2014, pp. 62–91.
doi:10.1017/jfm.2014.96

[14] Popov, P. P., Sideris, A., and Sirignano, W., "Uncertainty Quantification of Non-Linear Oscillation Triggering in a Multi-Injector Liquid Propellant Rocket Combustion Chamber," *67th APS/DFD Meeting*, The American Physical Soc., College Park, MD, 2014, Paper R21.00012.

[15] Morgan, C., "Response of a Gas-Gas Shear Coaxial Injector to Transverse Instability," M.S. Thesis, Purdue Univ., Lafayette, IN, 2012.

[16] Pomeroy, B., "Measurement and Analysis of Combustor Response to Transverse Combustion Instability," Ph.D. Thesis, Purdue Univ., Lafayette, IN, 2012.

[17] Shipley, K., Morgan, C., Anderson, W., Harvazinski, M., and Sankaran, V., "Computational and Experimental Investigation of Transverse Combustion Instabilities," *Joint Propulsion Conference*, AIAA Paper 2013-3992, 2013, pp. 1083–1099.

[18] Levine, R., "Experimental Status of High Frequency Liquid Rocket Combustion Instability," *Proceedings of the 10th (International) Symposium on Combustion*, The Combustion Inst., Pittsburgh, PA, 1965.
doi:10.1016/S0082-0784(65)80248-X

[19] Westbrook, C. K., and Dryer, F. L., "Chemical Kinetic Modeling of Hydrocarbon Combustion," *Progress in Energy and Combustion Science*, Vol. 1, No. 1, 1984, pp. 1–57.
doi:10.1016/0360-1285(84)90118-7

[20] Pierce, C., and Moin, P., "Progress-Variable Approach for Large-Eddy Simulation of Non-Premixed Turbulent Combustion," *Journal of Fluid Mechanics*, Vol. 504, 2004, pp. 73–97.
doi:10.1017/S0022112004008213

[21] Pope, S. B., *Turbulent Flows*, Cambridge Univ. Press, New York, 2000, pp. 289–290.

E. Kim
Associate Editor